

Chirality-induced linear response properties in non-coplanar Mn_3Ge

Sebastian Wimmer, Sergiy Mankovsky, Hubert Ebert¹

¹*Department Chemie, Physikalische Chemie, Universität München, Butenandtstr. 5-13, 81377 München, Germany*

Taking the non-collinear antiferromagnetic hexagonal Heusler compound Mn_3Ge as a reference system, the contributions to linear response phenomena arising solely from the chiral coplanar and non-coplanar spin configurations are investigated. Orbital moments, X-ray absorption, anomalous and spin Hall effects, as well as corresponding spin-orbit torques and Edelstein polarizations are studied depending on a continuous variation of the polar angle relative to the Kagome planes of corner-sharing triangles between the non-collinear antiferromagnetic and the ferromagnetic limits. By scaling the speed of light from the relativistic Dirac case to the non-relativistic limit the chirality-induced or topological contributions can be identified by suppressing the spin-orbit coupling.

I. INTRODUCTION

Chiral magnetic order, its origins and consequences, continues to be a fascinating area of current solid state science.^{1–5} Particularly intriguing is the occurrence of mesoscopic quasiparticles formed by a continuously varying non-coplanar spin texture with defined topology, so-called Skyrmions.^{6–8} Their properties, creation, as well as detection and manipulation is a very active field of research,^{9–14} motivated by potential future applicability in magnetic storage.^{15–18} Electric-field-induced transport plays an important role in this context, as corresponding charge and spin currents can be utilized to detect and manipulate Skyrmions^{15,16,19} and Antiskyrmions.²⁰ Due to the non-coplanar spin texture a so-called emergent electromagnetic field arises, that leads to chirality-induced or *topological*, in the sense of arising from the real-space topology of the spin configuration, contributions to phenomena commonly associated with spin-orbit coupling. The most fundamental of them are the occurrence of topological orbital moments^{21–26} and of the related topological Hall effect (THE).^{27–34} A corresponding spin Hall effect arising from the real-space topology of the spin texture³⁵ is of particular interest in antiferromagnetic skyrmions, where the THE vanishes.³⁶

A second intensively investigated type of chiral magnetic order is that of bulk antiferromagnets with non-collinear spin arrangements. The anomalous Hall effect (AHE) has been studied extensively in such compounds both theoretically^{21,31,37–39} and experimentally.^{40–46} Its relation to the magneto-optic Kerr effect of chiral magnets^{47,48} and the X-ray circular dichroism^{25,49}, both connected to the optical conductivity tensor, suggests an alternative, magneto-optical approach to non-collinear magnetic order. Of particular relevance to the field are the hexagonal Heusler compounds Mn_3X with $X = \text{Ga}, \text{Ge}, \text{and Sn}$, in which the AHE has recently been confirmed experimentally.^{42–44} Its spin-polarized counterpart, the spin Hall effect (SHE), in these and other non-collinear antiferromagnets also stimulated theoretical efforts^{39,50–52} and has been measured in the achiral cubic system Mn_3Ir .^{53,54} In Ref. 54 it has been furthermore shown, that the SHE contributes to the so-called spin-orbit torque (SOT), the current-induced magnetic

torque that can be utilized to efficiently switch the magnetization. Thermally-induced analogues to the AHE and SHE, the anomalous and spin Nernst effects have been studied in Mn_3X ($X = \text{Sn}, \text{Ge}, \text{Ga}$) from first principles using the Berry curvature approach and a Mott-like formula.⁵⁵ The anomalous Nernst effect could in fact be measured recently in Mn_3Sn .⁵⁶

The merger of these two fields called *topological antiferromagnetic spintronics*⁵⁷ aims to explore the potential of topologically protected quasiparticles with non-trivial real- or momentum-space topology. This work contributes to this by a first-principles study on the chirality-induced or topological contributions to orbital moments, X-ray absorption spectra, anomalous and spin Hall effect, as well as to spin-orbit torques and the closely related Edelstein effect (EE). Two coplanar non-collinear antiferromagnetic spin structures in Mn_3Ge , one chiral and the other achiral, will be used as basis for investigations on the impact of non-coplanarity by rotating the magnetic moments out of the Kagome planes. Scaling the speed of light allows assessing the topological contributions to the various effects in absence of spin-orbit coupling. This will be accompanied by an analysis of the corresponding symmetry-restricted response tensor shapes.

The manuscript is organized as follows: In section II the underlying methods used for obtaining the results in section III will be outlined. The crystallographic and magnetic structures will be discussed in section III A, including the corresponding symmetry-restricted tensor shapes for electrical and spin conductivity as well as spin-orbit torque and Edelstein polarization. Topological orbital moments and their signatures in X-ray absorption spectra are the subjects of sections III B and III C, respectively. The chirality-induced contributions to the anomalous and spin Hall effect will be discussed in section III D, corresponding results for the spin-orbit torque and the Edelstein effect will be presented in section III E. Finally, hypothetical non-coplanar antiferromagnets will be investigated in section III F. A brief summary and outlook will be made at the end (IV), additional information can be found in Appendix A.

II. METHODS

The space-time symmetry analysis of the linear response tensors for charge^{58,59} and spin conductivity⁵⁹, spin-orbit torque⁶⁰ and Edelstein polarization⁶¹ performed in this work is based on the magnetic space group determined using the software FINDSYM^{62,63}. Calculations for the corresponding linear response quantities have been done on the basis of Kubo's linear response formalism^{64–68}. These were done in a fully relativistic way using spin-polarized relativistic Korringa-Kohn-Rostoker (SPR-KKR)⁶⁹ electronic structure method within framework of the local spin density approximation (LSDA). Explicite expressions used for the calculations of the response functions can be found in the literature (charge conductivity^{64–66}, spin conductivity^{67,68}, spin-orbit torque⁶⁰, Edelstein effect⁶¹, X-ray absorption formalism⁷⁰). For the calculation of electric-field induced response properties the Kubo-Středa⁷¹ formula has been used throughout. To study the impact of the spin texture in absence of spin-orbit coupling, the non-relativistic limit of the Dirac formalism has been explored by scaling the speed of light.

III. RESULTS

A. Magnetic structure and symmetry

The hexagonal Mn_3Ge compound crystallizes, as its siblings Mn_3Sn and Mn_3Ga , in the D_{019} structure with space group $P6_3/mmc$. The non-magnetic unit cell is shown in Fig. 1 and will be labeled NM in the following. The Mn atoms on the Wyckoff positions $6h$ in the $\{0001\}$ planes colored in magenta (dark gray) form triangular, so-called Kagome lattices, stacked alternately along the $[0001]$ (z) direction. Ge atoms occupying the Wyckoff positions $2h$ are colored in light gray. Figure 2 shows the situation of a field-aligned ferromagnetic structure with all moments (only shown for Mn sites) oriented along the $[0001]$ or z direction (c axis of the unit cell). The corresponding magnetic space group is $P6_3/mm'c'$. This structure will be labeled FM in the following.

A number of non-collinear but coplanar antiferromagnetic alignments of the moments have been discussed for Mn_3Ge and related compounds in the literature (cf. Ref. 73 and references therein). Recently an overview on the properties of actual and hypothetical spin-compensated configurations has been given by the present authors.⁴⁹ Two coplanar ones of these structures discussed therein, both hypothetical, are shown in Fig. 3. The one in the upper panel, labeled ncAFM0, has the moments in the two alternating Kagome planes, indicated by different colors (red and blue), pointing towards the center of the triangles formed by the Mn atoms. The two magnetic sub-lattices are connected, e.g., by a 6_3 screw rotation about an axis going through the center of both triangles, but also by inversion with respect to

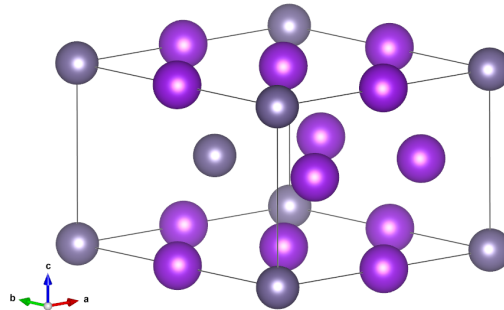


FIG. 1. Hexagonal unit cell of Mn_3Ge with space group $P6_3/mmc$ (labeled NM in the following). The Mn atoms on the Wyckoff positions $6h$ are colored in magenta (dark gray) and Ge atoms (Wyckoff positions $2h$) are colored in light gray.⁷²

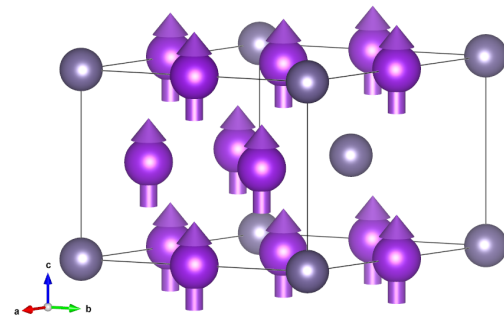


FIG. 2. Unit cell of hexagonal ferromagnetic (FM) Mn_3Ge with magnetic space group $P6_3/mm'c'$. Use of colors as in Fig. 1, magnetic moments on Mn sites are indicated as vectors.⁷²

the midpoint between these centers followed by time reversal. Reversing all moments in one layer (here blue), one obtains the structure ncAFM9 shown in the bottom panel. Here the operation connecting the two sub-lattices involves an additional time-reversal ($6'_3$), leading to a centrosymmetric or achiral structure with an inversion center half-way along c . Both structures will serve as references for the investigations on the consequences of non-coplanarity of the Mn moments in this work.

Rotation of the moments out of both Kagome planes by the same polar angle θ between the $[0001]$ direction and the $\{0001\}$ planes leads for $\theta = 45^\circ$ to the non-coplanar spin arrangements depicted in Fig. 4. The one in the upper panel, ncpM0 derived from ncAFM0, is obviously still chiral. The structure derived from ncAFM9, labeled ncpM9 and shown in the lower panel of Fig. 4 accordingly

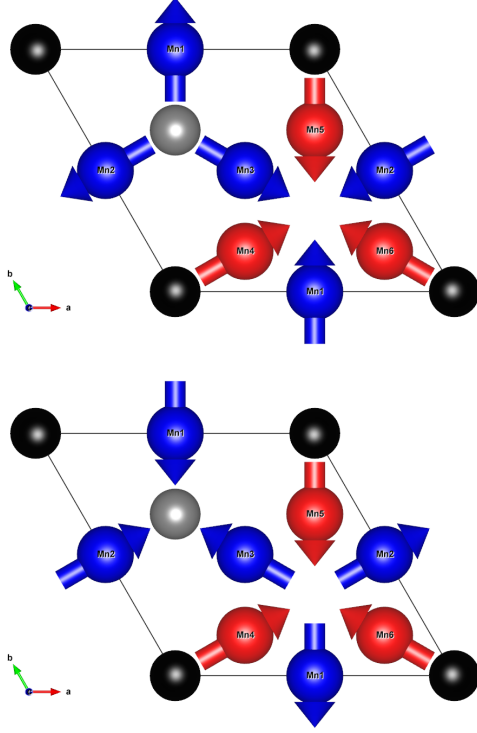


FIG. 3. Non-collinear coplanar (nc) antiferromagnetic reference structures of Mn_3Ge , ncAFM0 (top) and ncAFM9 (bottom). The coplanar Mn moments in alternating Kagome planes are colored red and blue. The achiral structure ncAFM9 in the lower panel is obtained from ncAFM0 by reversing all moments in one plane (blue).⁷²

remains achiral, the inversion center connecting the two sub-lattices is indicated by an orange dot.

The main aim of the present work is the numerical study of chirality-induced or *topological* effects in transport and related properties. While the individual Kagome sub-lattices in the antiferromagnetic structures just discussed are chiral, as they have a finite vector spin chirality $\vec{S}_i \times \vec{S}_j + \vec{S}_j \times \vec{S}_k + \vec{S}_k \times \vec{S}_i$, the anomalous Hall conductivity arising from this is vanishing globally. This can be unambiguously derived from the space-time symmetry properties of the current-current correlation function in terms of the Kubo formula behaviour for the electrical conductivity.⁵⁸ The transformation under all symmetry operations of the so-called magnetic Laue group (see Ref. 59 for its definition used here) is sufficient to derive the symmetry restricted tensor shape. The magnetic space and Laue groups for all spin configurations discussed in this work are given in Table. I. For convenience the Laue group is given also according to the older definition used by Kleiner⁵⁸.

The electrical conductivity tensor shapes derived from the corresponding magnetic Laue group are as

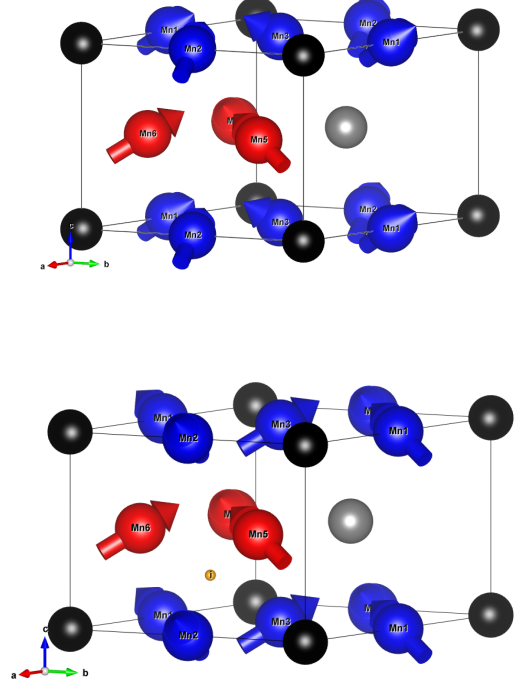


FIG. 4. Non-coplanar (ncp) magnetic structures of Mn_3Ge derived from ncAFM0 and ncAFM9 (see Fig. 3) by rotating the moments out of the Kagome planes by $\theta = 45^\circ$. While the one in the top panel, labeled ncpM0, is chiral, the structure ncpM9 in the bottom panel has an inversion center that is indicated by an orange dot.⁷²

label	MSG	MPG	MLG
NM	$P6_3/mmc1'$	$6/mmm1'$	$6/mmm1'$ (6221')
FM	$P6_3/mm'c'$	$6/mm'm'$	$6/mm'm'$ (62'2')
ncAFM0	$P6_3/m'm'c'$	$6/m'm'm'$	$6/mmm1'$ (6221')
ncAFM9	$P6_3'/m'm'c$	$6'/m'm'm$	$6'/m'm'm$ (6'22')
ncpM0	$P6_3m'c'$	$6m'm'$	$6/mm'm'$ (62'2')
ncpM9	$P\bar{3}m'1$	$\bar{3}m'1$	$\bar{3}m'1$ (32')
ncpAFM0	$P\bar{3}'1m'$	$\bar{3}'1m'$	$\bar{3}1m1'$ (3'2)
ncpAFM9	$P6_3'm'c$	$6'm'm$	$6'/m'm'm$ (6'2'2)

TABLE I. Magnetic space (MSG), point (MPG) and Laue groups (MLG) of the magnetic structures shown in Figs. 3 and 4 with nc and ncp standing for non-collinear and non-coplanar, respectively. The Laue groups are given following the standard definition used by Seemann *et al.*⁵⁹ as well as the older one used by Kleiner⁵⁸ (in parentheses). The conventional setting concerning the sequence of generators is used for the space groups and carried over to the point and Laue groups.⁷⁴

follows:^{58,59}

$$\underline{\sigma}^{\text{NM}} = \begin{pmatrix} \sigma_{xx} & 0 & 0 \\ 0 & \sigma_{xx} & 0 \\ 0 & 0 & \sigma_{zz} \end{pmatrix} = \underline{\sigma}^{\text{ncAFM0,9}} = \underline{\sigma}^{\text{ncpAFM0,9}} \quad (1)$$

$$\underline{\sigma}^{\text{FM}} = \begin{pmatrix} \sigma_{xx} & \sigma_{xy} & 0 \\ -\sigma_{xy} & \sigma_{xx} & 0 \\ 0 & 0 & \sigma_{zz} \end{pmatrix} = \underline{\sigma}^{\text{ncpM0,9}}. \quad (2)$$

As stated above, the non-collinear coplanar antiferromagnetic structures in Fig. 3 have the same conductivity tensor shape as the non-magnetic one. This applies as well to the non-coplanar antiferromagnetic structures that will be discussed in Section III F. The non-coplanar magnetic structures of Fig. 4 on the other hand have the same shape of $\underline{\sigma}$ as for the ferromagnetic (FM) case. However, as will be shown below, a chirality-induced contribution to the anomalous Hall conductivity $\sigma_{xy} = -\sigma_{yx}$ can be identified here.

The corresponding spin conductivity tensor shapes for polarization along the z or $[0001]$ direction are:⁵⁹

$$\underline{\sigma}^{z,\text{NM}} = \begin{pmatrix} 0 & \sigma_{xy}^z & 0 \\ -\sigma_{xy}^z & 0 & 0 \\ 0 & 0 & 0 \end{pmatrix} = \underline{\sigma}^{z,\text{ncAFM0,9}} = \underline{\sigma}^{z,\text{ncpAFM0,9}} \quad (3)$$

$$\underline{\sigma}^{z,\text{FM}} = \begin{pmatrix} \sigma_{xx}^z & \sigma_{xy}^z & 0 \\ -\sigma_{xy}^z & \sigma_{xx}^z & 0 \\ 0 & 0 & \sigma_{zz}^z \end{pmatrix} = \underline{\sigma}^{z,\text{ncpM0,9}}. \quad (4)$$

The corresponding tensor for polarization along the x - and y -direction can be found in Ref. 59. The antiferromagnetic structures, regardless whether coplanar or non-coplanar, chiral or achiral, show only one independent non-zero element, namely the spin Hall conductivity $\sigma_{xy}^z = -\sigma_{yx}^z$ as in the non-magnetic case. Note however, that the tensors for the other two polarization directions differ for the structures ncAFM9, ncpAFM0, and ncpAFM9 (see Ref. 59). The non-coplanar magnetic structures ncpM0 and ncpM9 have the same tensor shape for $\underline{\sigma}^z$ as the ferromagnetic one. While ncpM0 has the same magnetic Laue group ($6/m\bar{m}'m'$) and accordingly the same tensor shapes for all $\underline{\sigma}^k$ as the FM structure, the other two polarization directions, x and y , behave again differently for ncpM9. Also here a sizable chirality-induced contribution will be shown to exist.

The Edelstein polarization tensor shapes for the non-centrosymmetric spin configurations ncAFM0, ncpM0, ncpAFM0, and ncpAFM9 are found as follows:⁶¹

$$\underline{p}^{\text{ncAFM0}} = \begin{pmatrix} p_{xx} & 0 & 0 \\ 0 & p_{xx} & 0 \\ 0 & 0 & p_{zz} \end{pmatrix} \quad (5)$$

$$\underline{p}^{\text{ncpM0}} = \begin{pmatrix} p_{xx} & p_{xy} & 0 \\ -p_{xy} & p_{xx} & 0 \\ 0 & 0 & p_{zz} \end{pmatrix} \quad (6)$$

$$\underline{p}^{\text{ncpAFM0}} = \begin{pmatrix} p_{xx} & 0 & 0 \\ 0 & p_{xx} & 0 \\ 0 & 0 & p_{zz} \end{pmatrix} \quad (7)$$

$$\underline{p}^{\text{ncpAFM9}} = \begin{pmatrix} 0 & p_{xy} & 0 \\ -p_{xy} & 0 & 0 \\ 0 & 0 & 0 \end{pmatrix}. \quad (8)$$

Finally, the shapes of the spin-orbit torque tensors \underline{t} are identical to the ones given for \underline{p} in Eqs. (5)-(8)⁶⁰. It should be stressed that for these two response properties the tensor shape is determined by the magnetic point group and not by the magnetic Laue group.

B. Orbital moments

The occurrence of chirality-induced orbital moments in non-coplanar spin arrangements has been predicted already quite some time ago.^{21,22} First-principles calculations in, e.g., atomic-scale spin lattices^{23,24}, tri-atomic clusters of ferromagnetic 3d-elements on a surface²⁵, and bulk γ -FeMn²⁶ could verify these in the limit of vanishing spin-orbit coupling. The (non-)coplanarity between three spins can be expressed compactly by the so-called scalar spin chirality $\chi_{ijk} = \vec{S}_i \cdot (\vec{S}_j \times \vec{S}_k)$. If the volume of the parallelepiped spanned by the three spin vectors is non-zero, they obviously are non-coplanar. In Figure 5 the orbital moment μ_{orb} ⁷⁵ is shown for ncpM0 as a function of the polar angle θ between the $[0001]$ direction and the $\{0001\}$ planes. Here μ_{orb} is defined as the modulus of the vector sum over all sites in the unit cell that leads to the effective orbital moment along the z direction. In case of vanishing spin-orbit coupling (no SOC, red open circles) the remaining chirality induced contribution to the orbital moment can indeed be fairly well fitted with a function $\propto \cos(\theta) \sin^2(\theta)$ reflecting the scalar spin chirality $\chi_{ijk}(\theta)$. The zeros of this function correspond to the ferromagnetic state ($\theta = 0^\circ, 180^\circ$) and the non-collinear antiferromagnetic state ($\theta = -90^\circ, 90^\circ, 270^\circ$). The extremal values are found for integer multiples of $\theta = \arccos(1/\sqrt{3}) \approx 54.7356^\circ$, i.e., for the *magic angle*.

Figure 6 shows spin and orbital moments for the structure ncpM9 as a function of polar angle θ , again with and without spin-orbit coupling. For the spin moment (black squares) spin-orbit coupling is, as to be expected, of negligible relevance. The orbital moment (red circles) again has a large chirality-induced component, whose angular dependence however does not appear to be simply proportional to the scalar spin chirality. While the even symmetry about $\theta = 0^\circ$ and the odd symmetry around

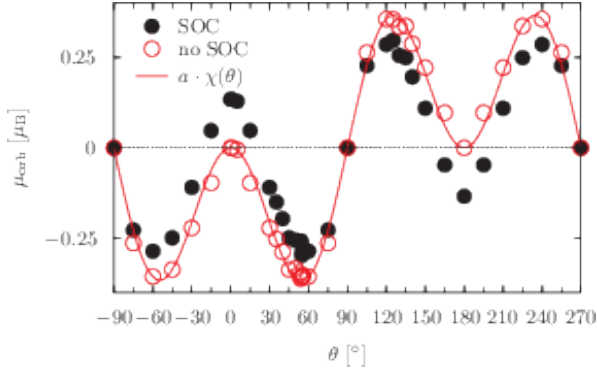


FIG. 5. Orbital moment as a function of polar angle θ in the non-coplanar chiral magnet ncpM0. Results including spin-orbit coupling (SOC) are shown as full (black) circles, those for vanishing SOC are given as open (red) circles. A fit of the latter to the scalar spin chirality $\chi(\theta)$ (see text) is shown as solid (red) line.

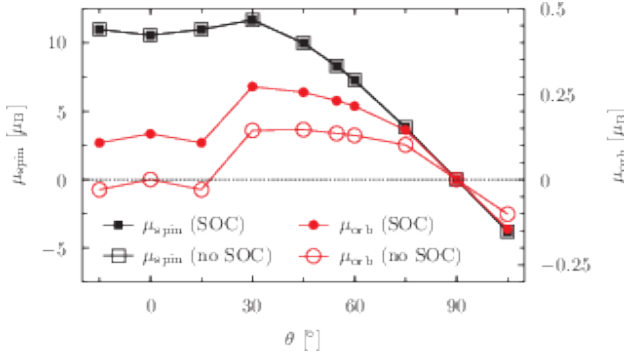


FIG. 6. Spin and orbital moment as a function of polar angle θ in the non-coplanar achiral magnet ncpM9. Results including spin-orbit coupling (SOC) are shown as full symbols, those for vanishing SOC are given as open symbols.

$\theta = 90^\circ$ is obeyed, the behavior in-between seems to be more complicated. Note that, despite the global inversion symmetry connecting the two Kagome sub-lattices, these have, as in the case of ncpM0, the same finite scalar spin chirality.

C. X-ray absorption spectra

X-ray absorption spectroscopy has a long and successful history concerning its application as a local probe to magnetic systems. In particular the so-called XMCD sum rules^{76–78} allow for example to deduce from the integrated $L_{2,3}$ -spectra of 3d-transition metals their spin and orbital magnetic moments. In line with the sum rules an angular dependence according to $\cos(\hat{m} \cdot \hat{q})$ is normally assumed, where \hat{m} and \hat{q} are the orientation of the local moment probed by XMCD and of the X-ray beam, respectively. This simple relation implies that in

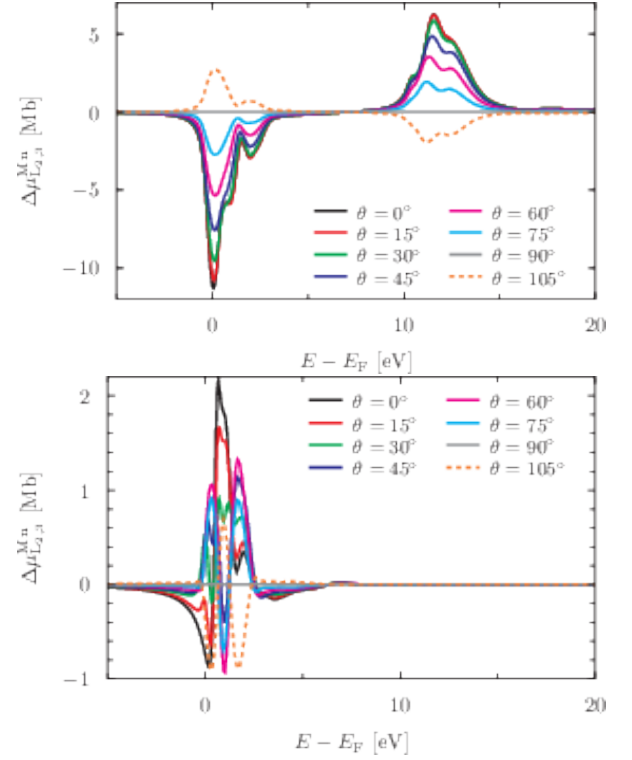


FIG. 7. X-ray magnetic circular dichroism (XMCD) spectra $\Delta\mu_{L_{2,3}}^{Mn}$ at the Mn $L_{2,3}$ -edge in the non-coplanar chiral magnetic structure ncpM0 with (top) and without (bottom) inclusion of spin-orbit coupling (SOC). The polar angle θ gives the tilt of the moments w.r.t. the $[0001]$ direction, that coincides with the direction of the X-ray beam.

spin-compensated antiferromagnetic systems the XMCD should vanish. However, both XMCD⁴⁹ as well as the magneto-optic Kerr effect (MOKE)^{37,47} are in fact, due to their relation to the frequency-dependent conductivity tensor,⁷⁰ expected to be observable in any magnetic structure that allows for a finite anomalous Hall conductivity.

In order to elucidate whether also the chirality-induced orbital moment discussed in Section III B can be deduced from X-ray absorption as suggested by Dos Santos Dias *et al.*²⁵, we perform first-principles calculations of XAS spectra as a function of polar angle θ . The XMCD signals in the non-coplanar magnetic structure ncpM0 including and excluding spin-orbit coupling is shown in Figure 7 in the top and bottom panels, respectively. The absorption for incidence along the $[0001]$ direction is calculated for the $L_{2,3}$ -edge of Mn and summed over all sites of the unit cell. Suppressing spin-orbit coupling obviously leads to a degeneracy of the $2p$ initial states, i.e. it removes in particular the spin-orbit splitting into $2p_{1/2}$ - and $2p_{3/2}$ -shells. Accordingly only one edge is visible in the lower panel, that nevertheless shows an XMCD signal. In both cases the strength of the signal is decreasing with increasing θ and anti-symmetric w.r.t. reversal of the global z

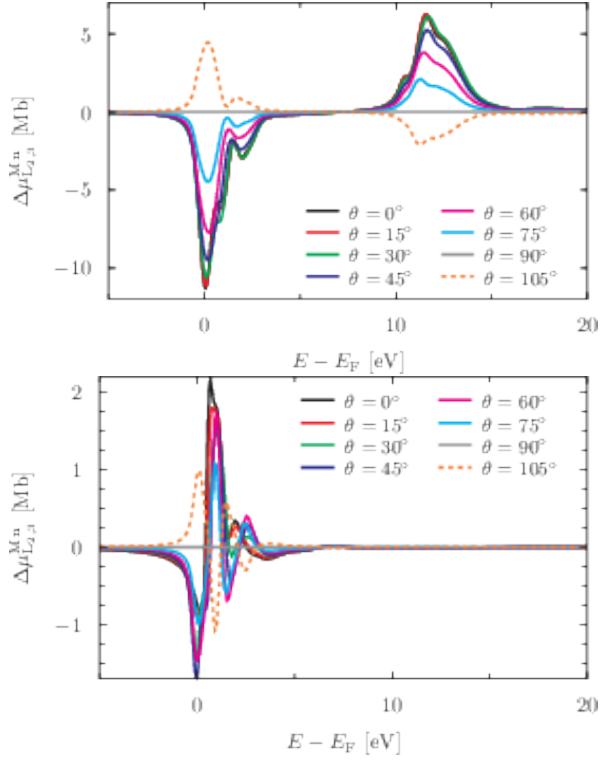


FIG. 8. X-ray magnetic circular dichroism (XMCD) spectra $\Delta\mu_{L_{2,3}}^{Mn}$ at the Mn $L_{2,3}$ -edge in the non-coplanar achiral magnetic structure ncpM9 with (top) and without (bottom) inclusion of spin-orbit coupling (SOC). The polar angle θ gives the tilt of the moments w.r.t. the $[0001]$ direction, that coincides with the direction of the X-ray beam.

component of the magnetization. The same applies to the XMCD spectra for the achiral structure ncpM9 in Fig. 8. Here the fine structure at the L_2 -edge is slightly different from that in ncpM0 for the fully relativistic spectra in the top panel and quite so for the non-relativistic ones in the bottom panel.

As the XMCD signal is determined by both spin and orbital magnetic moment, a clear-cut decomposition is desirable in order to assess the chirality-induced contribution to the latter by X-ray absorption spectroscopy. Since the standard XMCD sum rules cannot be applied here and their generalization to non-collinear magnetic order is still an open issue, an approximate scheme following the proposal in Ref. 25 has been employed. Figures 9 and 10 show the difference between the average XAS and the XMCD signals for the field-aligned (ferromagnetic, FM, $\theta = 0^\circ$) limit and the non-collinear structures with $\theta \neq 0^\circ$ in ncpM0 and ncpM9, respectively. As stated above, this follows the proposed protocol of Dos Santos Dias *et al.*,²⁵ devised for magneto-optical experiments on skyrmionic systems. A remaining obstacle is however the assessment of the spin-moment-induced contribution for which a linear and spin texture-independent relation to the polar angle has been assumed by these authors. Ob-

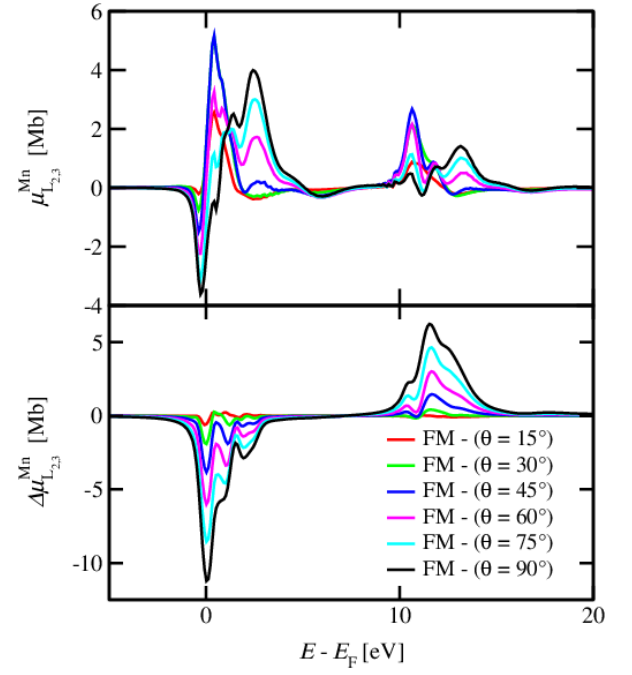


FIG. 9. Difference between ferromagnetic and non-collinear polarization-averaged XAS spectra (top) and X-ray magnetic circular dichroism (XMCD) spectra (bottom) at the Mn $L_{2,3}$ -edge in the chiral magnetic structure ncpM0. The polar angle θ gives the tilt of the moments w.r.t. the $[0001]$ direction.

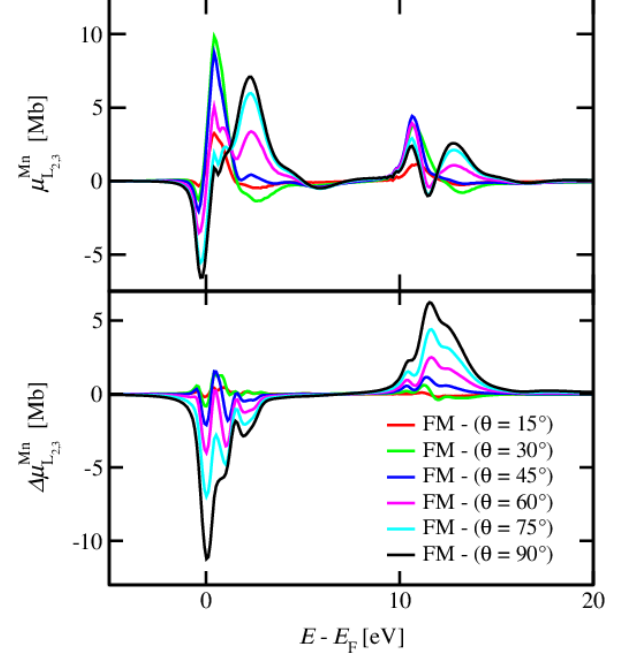


FIG. 10. Difference between ferromagnetic and non-collinear polarization-averaged XAS spectra (top) and X-ray magnetic circular dichroism (XMCD) spectra (bottom) at the Mn $L_{2,3}$ -edge in the achiral magnetic structure ncpM9. The polar angle θ gives the tilt of the moments w.r.t. the $[0001]$ direction.

viously an unambiguous separation into spin- and orbital as well as spin-orbit- and chirality-induced contributions is duly needed. Note that due to the simplified assumption of a collinear arrangement of moments the standard XMCD rules certainly have to be revised in order to make full use of the proposed procedure.

D. Transport results: (T)AHE and (T)SHE

Results for the anomalous Hall conductivity σ_{xy} as a function of θ are shown in the top panel of Fig. 11 for ncpM0. As can be seen both AHC and the chirality-induced or topological contribution σ_{xy}^T obtained in the non-relativistic limit $c_0/c \rightarrow 0$ (see Appendix A) are anti-symmetric or odd w.r.t. magnetization reversal around $\theta = 90^\circ$. The chirality-induced component is clearly not simply proportional to the scalar spin chirality (see Fig. 5), similar to the observation made by Hanke *et al.*²⁶ for γ -FeMn. The largest values for σ_{xy}^T are for example found for $\theta = 60^\circ$ and 120° and not for the magic angle. In addition we observe two sign changes between the coplanar antiferromagnetic structure ($\theta = 90^\circ$) and the ferromagnetic states at $\theta = 0^\circ$ and 180° . In these limits σ_{xy}^T vanishes and the AHC is purely spin-orbit-induced. Note, that the calculations were performed for the finite temperature $T = 300$ K that was accounted for by uncorrelated lattice displacements via the so-called alloy analogy model (AAM).⁷⁹ This was done in order to circumvent the numerical difficulties arising for the \vec{k} -space integration for perfectly ordered systems. However, as it turns out, the conductivities are almost entirely intrinsic in nature in the sense of negligible impact of the so-called vertex corrections associated with the thermally-induced disorder. Accordingly it is the magnetic band structure that determines the angular dependence of the AHC, or expressed alternatively its Berry curvature^{80,81} as skew scattering contributions arising from the presence of impurities⁸² or locally correlated fluctuating spins⁸³ are not considered here. The spin Hall conductivity in the relativistic and non-relativistic limits, σ_{xy}^z and $\sigma_{xy}^{z,T}$, given in the lower panel of Fig. 11 is even w.r.t. magnetization reversal around antiferromagnetic configuration at $\theta = 90^\circ$. It is strongly dependent on the non-coplanar spin texture and quite differently so for its spin-orbit- and chirality-induced contributions. These can be of the same or of different sign, leading to partial or even nearly complete cancellation as for $\theta \approx 54.7356^\circ$. Quite interestingly, at $\theta = 105^\circ$ both appear to vanish. Note that in the ferromagnetic limit at $\theta = 0^\circ$ and 180° the total value is small but non-zero, while the topological contribution $\sigma_{xy}^{z,T}$ vanishes.

Quite similar observations can be made in Fig. 12 for the achiral spin structure ncpM9 shown for the range $\theta = -15 - 105^\circ$. As can be seen, the AHC in the top panel is found to be anti-symmetric (odd) w.r.t. magnetization reversal whereas the SHC in the bottom panel is symmetric. The detailed angular dependence is distinct

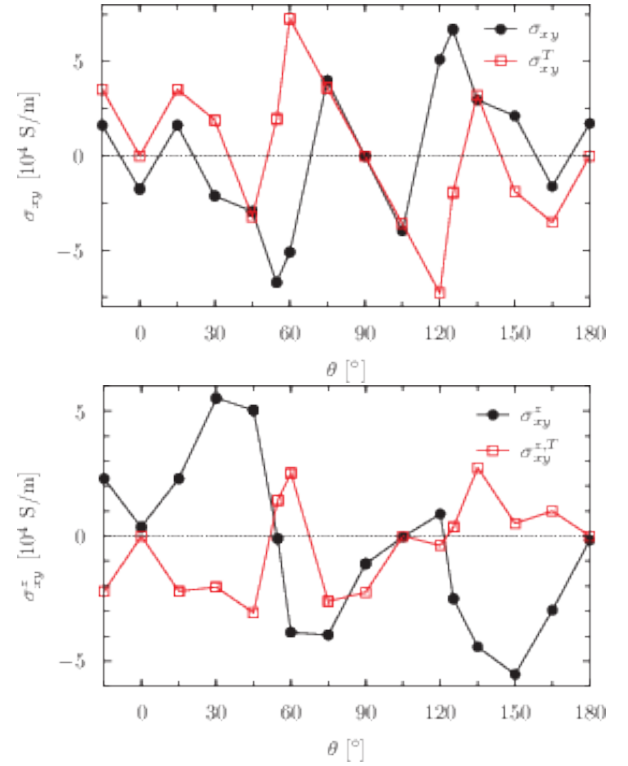


FIG. 11. Top: Anomalous Hall conductivity σ_{xy} and its chirality-induced or topological contribution σ_{xy}^T as functions of polar angle θ in ncpM0. Bottom: Corresponding results for the (topological) spin Hall conductivity σ_{xy}^z ($\sigma_{xy}^{z,T}$).

from that in ncpM0 for both quantities, i.e., the two hypothetical structures could be distinguished experimentally. We propose that the abundance of assumed spin configurations in hexagonal Mn_3X compounds could be confirmed or discarded via corresponding transport measurements rotating an applied magnetic field supported together with accompanying first-principles calculations.

The longitudinal charge transport is even w.r.t. magnetization reversal and anisotropic, i.e., $\sigma_{xx} = \sigma_{yy} \neq \sigma_{zz}$. In the absence of spin-orbit coupling and the associated anisotropic magneto-resistance, the anisotropy of the spin texture as well as the bare crystal-induced anisotropy already present in the non-magnetic case remain. Similar observations can be reported for the longitudinal spin conductivities $\sigma_{xx}^z = \sigma_{yy}^z \neq \sigma_{zz}^z$, that however are not fully even w.r.t. magnetization reversal. The spin conductivity tensor elements for the other spin polarizations either show large chirality-induced contributions as well ($\sigma_{xy}^k = -\sigma_{yx}^k$ with $k = \{x, y\}$) or are exclusively SOC-induced ($\sigma_{iz}^k \neq -\sigma_{zi}^k$ with $i \neq k = \{x, y\}$). Note that all of them are even w.r.t. magnetization reversal.

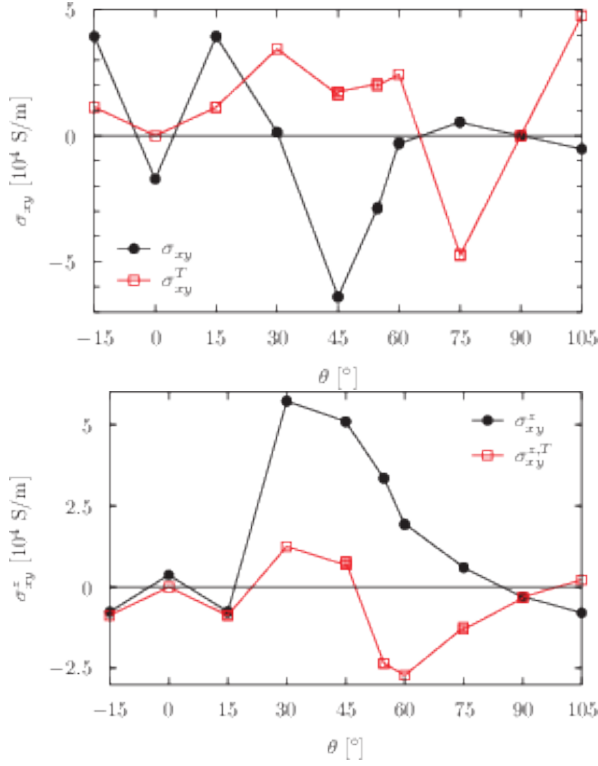


FIG. 12. Top: Anomalous Hall conductivity σ_{xy} and its chirality-induced or topological contribution σ_{xy}^T as functions of polar angle θ in ncpM9. Bottom: Corresponding results for the (topological) spin Hall conductivity σ_{xy} ($\sigma_{xy}^{z,T}$).

E. Spinorbitronic effects: (T)SOT and (T)EE

Naturally the question arises whether the so-called spinorbitronic phenomena spin-orbit torque (SOT) and Edelstein effect (EE) also exhibit chirality-induced contributions leading to finite values in the absence of spin-orbit coupling. Employing the same Kubo linear response framework used for the charge and spin transport calculations in the previous section, but exchanging the operator for the response, the (spin) current density operators, by either the magnetic torque operator⁶⁰ or the spin magnetization operator⁶¹, the torkances t_{ij} and Edelstein polarizations p_{ij} can be computed from first principles. Figure 13 shows the polar-angle dependence of the torkance tensor elements $t_{xx} = t_{yy}$ (top), $t_{xy} = -t_{yx}$ (middle), and t_{zz} (bottom) in the chiral compound ncpM0. The diagonal torkances in the top and bottom panels are obviously even w.r.t. magnetization reversal, i.e., anti-symmetric w.r.t. $\theta = 90^\circ$, while the off-diagonal anti-symmetric element $t_{xy} = -t_{yx}$ in the middle panel is odd. For this as well as for the $t_{xx} = t_{yy}$ indeed a sizable chirality-induced contribution is found that appears to be largest at $\theta = 30^\circ$ and 150° . The diagonal torkance t_{zz} in the bottom panel, corresponding to a rotation of the moments about the [0001] or z axis coinciding with the direction of the applied electric

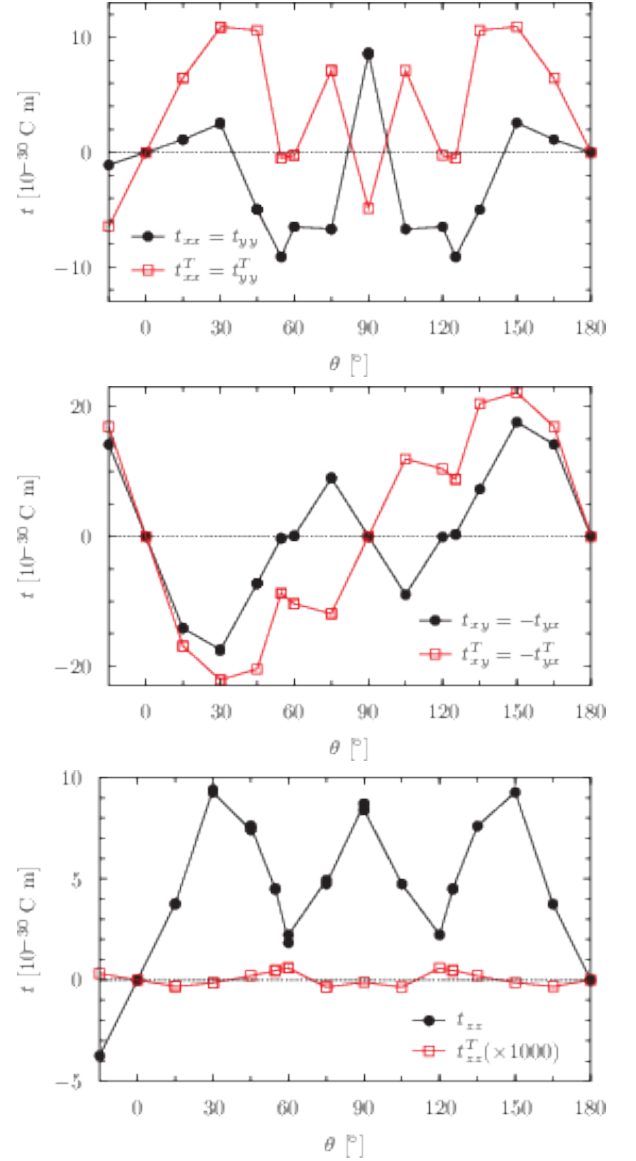


FIG. 13. Spin-orbit torkances $t_{xx} = t_{yy}$ (top), $t_{xy} = -t_{yx}$ (middle), and t_{zz} (bottom) as functions of polar angle θ in ncpM0. The chirality-induced contributions t_{ij}^T are given as red open squares.

field, is almost exclusively spin-orbit-driven. In all three cases the full torkances vanish in the ferromagnetic limit ($\theta = 0^\circ$ and 180°) due to inversion symmetry.

The Edelstein polarization is one of the two microscopic mechanisms usually discussed as a source for the SOT, namely the (Rashba-)Edelstein torque, while the spin-Hall torque is attributed to the spin-transfer-torque-like action of a spin-polarized current on the local magnetization. The elements of the corresponding Edelstein polarization tensor \mathbf{p} are shown in Fig. 14 as a function of the polar angle θ . The elements p_{ij} are found to behave very similar to the corresponding elements of \mathbf{t} , i.e., the diagonal elements are even, the off-diagonal ones are

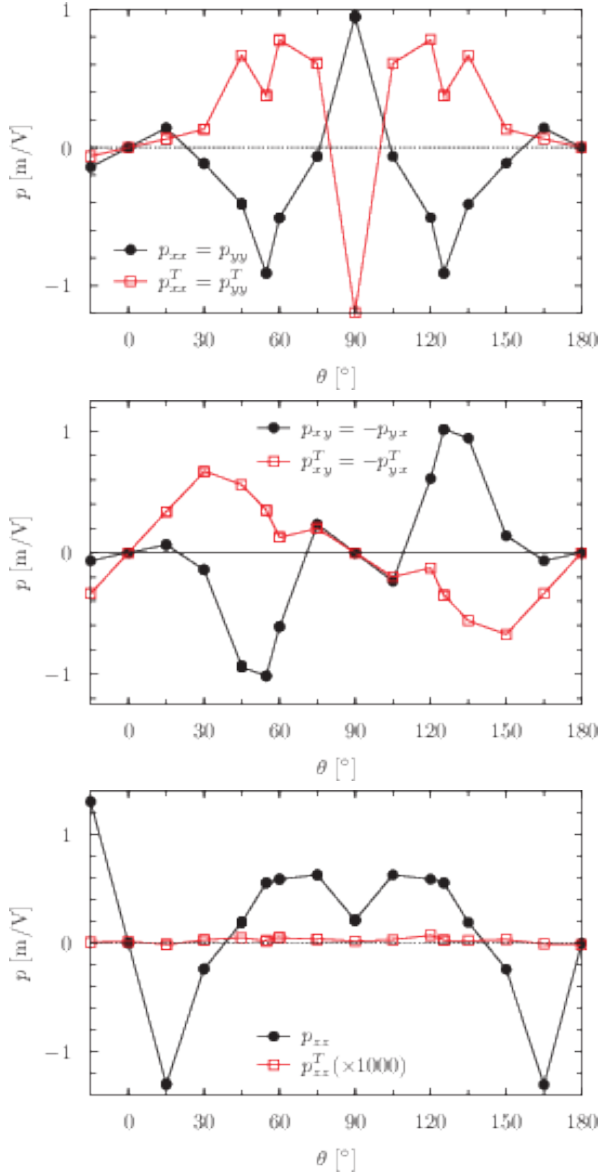


FIG. 14. Edelstein polarization tensor elements $p_{xx} = p_{yy}$ (top), $p_{xy} = -p_{yx}$ (middle), and p_{zz} (bottom) as functions of the polar angle θ in ncpM0. The small chirality-induced contributions p_{ij}^T scaled by the factor 1000 are given as red open squares.

odd, and $p_{xx} = p_{yy}$ (top) as well as $p_{xy} = -p_{yx}$ (middle) are overall chirality-dominated while p_{zz} in the bottom panel is again essentially SOC-induced. Note however, that the correspondence between t_{ij} and p_{ij} is not trivial, as an additional crossproduct with the local magnetization is involved for the operator representing the response in the case of the torkance. This leads for example for the odd torkance $t_{xy} = -t_{yx}$ in the middle panel of Fig. 13 to a different angular dependence as compared to $p_{xy} = -p_{yx}$ in particular close to the ferromagnetic limits at the left and right ends. For the topological con-

tributions this is even more pronounced. While the odd Edelstein polarization is chirality-dominated close to the antiferromagnetic configuration at $\theta = 90^\circ$, the SOT- and chirality-induced torkances are even of different sign here. The achiral coplanar and non-coplanar structures ncAFM9 and ncpM9 are found to be numerically zero as demanded by the inversion symmetry (see Section III A).

F. Non-coplanar antiferromagnets

By rotating the moments in the two Kagome planes in opposite directions by the same angle θ , non-coplanar antiferromagnetic structures as shown in Fig. 15 for $\theta = \pm 45^\circ$ are obtained. The upper panel is derived from the co-planar AFM structure ncAFM0, while the ncpAFM9 structure in the lower panel is obtained from the achiral ncAFM9 structure. As θ differs for both magnetic sub-lattices, the inversion symmetry is obviously broken, i.e., a chiral structure results. Note, that for ncpAFM0 inversion combined with time-reversal ($\bar{1}'$) is still a symmetry operation.

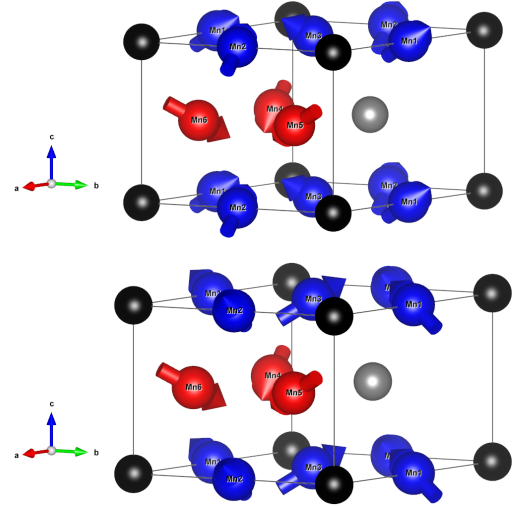


FIG. 15. Non-coplanar antiferromagnetic structures obtained from Fig. 3 by rotating the moments in the two Kagome planes into opposite directions by the same angle. The structure in the top panel has the same chirality in both sub-lattices (ncpAFM0), while in the lower panel they are of opposite sign (ncpAFM9).⁷²

The tensor shapes for charge and z -polarized spin conductivity correspond for both structures to the non-magnetic case, i.e., they are diagonal with $\sigma_{xx} = \sigma_{yy} \neq \sigma_{zz}$ and only one independent element of σ^z , the spin Hall conductivity $\sigma_{xy}^z = -\sigma_{yx}^z$. The shapes of σ^x and σ^y for ncpAFM0 and ncpAFM9, however, differ from each other as well as from the ones for the NM structure.⁵⁹ For the torkance and the Edelstein polarization the tensor shapes are given in Eqs. (7) and (8). Obviously there is a fi-

nite Edelstein polarization as well as spin-orbit torque present for both structures. However, the corresponding tensor shapes differ from each other, as the magnetic point group has to be considered here.^{60,61}

Figure 16 shows the Edelstein polarization tensor elements p_{xx} , p_{xy} , and p_{zz} for both structures at $\theta = \pm 45^\circ$ as a function of a scaled speed of light c (see Appendix A for details). Confirming the tensor shapes in Eqs. (7)

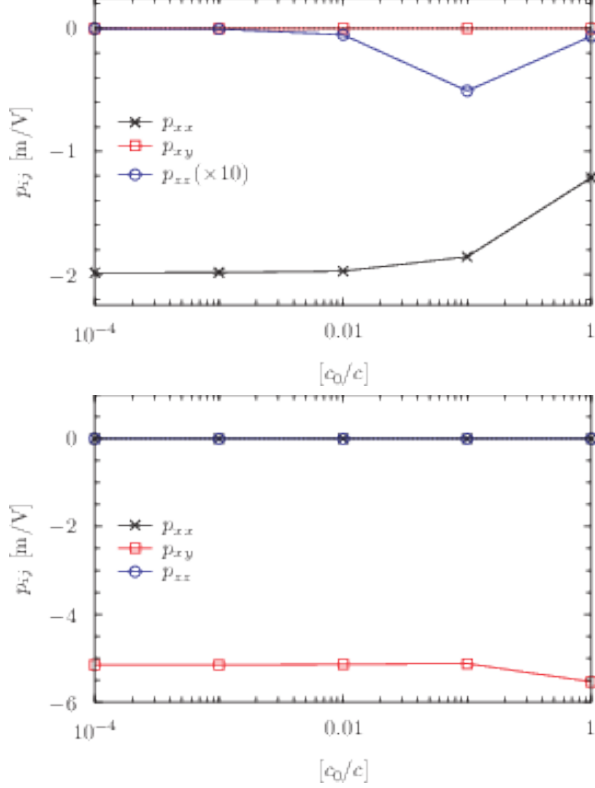


FIG. 16. Edelstein polarizations p_{xx} , p_{xy} , and p_{zz} in ncpAFM0 (top) and ncpAFM9 (bottom) as function of c_0/c . For both structures the polar angle θ is 45° . The relativistic limit is on the right ($c_0/c = 1$), the non-relativistic one on the left ($c_0/c \rightarrow 0$).

and (8), in the upper panel only the diagonal elements are non-zero, while in the lower panel only p_{xy} is non-vanishing. Furthermore it can be stated that for ncpAFM0 again p_{zz} is smaller than p_{xx} and vanishes in the non-relativistic limit ($c_0/c \rightarrow 0$), while p_{xx} has a large chirality-induced contribution. The anti-symmetric Edelstein polarization p_{xy} for ncpAFM9 shown in the bottom panel of Fig. 16 is even almost exclusively arising from the spin texture.

In agreement with the absence of off-diagonal anti-symmetric conductivity tensor elements the XMCD signals of the two chiral magnetic sub-lattices cancel each other numerically exactly (not shown here). The same applies to the anomalous Hall conductivity shown in Fig. 17, while the spin Hall conductivities are found to be finite with sizable topological contributions.

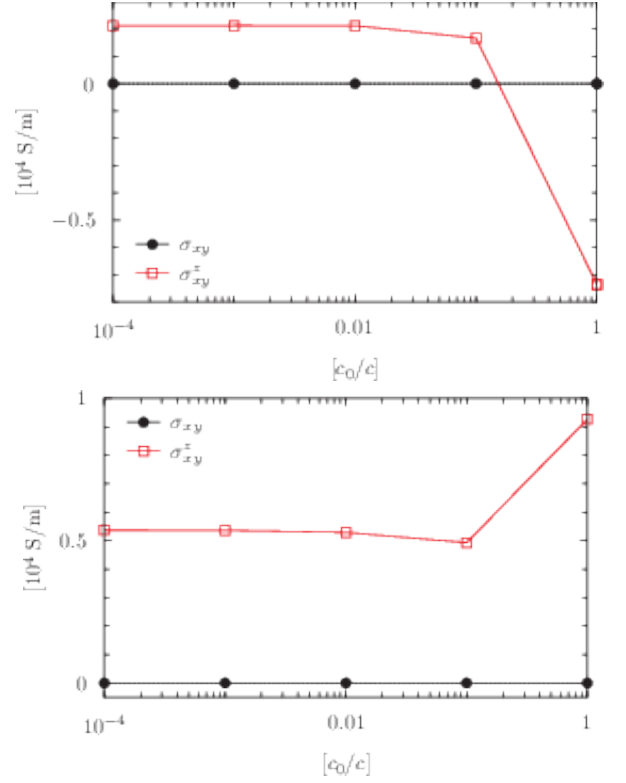


FIG. 17. Anomalous and spin Hall conductivities, σ_{xy} and σ_{xy}^z , respectively, in ncpAFM0 (top) and ncpAFM9 (bottom) as functions of c_0/c . For both structures the polar angle θ is 45° . The relativistic limit is on the right ($c_0/c = 1$), the non-relativistic one on the left ($c_0/c \rightarrow 0$).

IV. CONCLUSIONS

To summarize, the effect of a non-collinear and non-coplanar spin texture on orbital moments, X-ray absorption, charge and spin transport as well as spin-orbit torque and Edelstein polarization has been investigated by first-principles calculations for hexagonal Mn_3Ge . By smoothly varying the polar angle w.r.t. to the Kagome planes of corner-sharing triangles in two hypothetical reference structures, one globally chiral one achiral, the chirality-induced or topological contributions are compared to the spin-orbit-induced parts. To obtain the former in absence of the latter, the non-relativistic limit has been taken by scaling the speed of light c . The key findings are first of all the occurrence of topological orbital moments in presence and absence of global inversion symmetry, in the latter case following the angular dependence expected from the scalar spin chirality. A proposal of its experimental verification by XMCD measurements in a rotating external magnetic field is supported by a comparison of spectra for the field-aligned ferromagnetic case with those of non-coplanar spin configurations. Also here the limit of vanishing spin-orbit coupling has been investigated, conclusive statements could however

not yet been made due to limitations of the standard XMCD sum rules. Furthermore the presence, angular dependence, as well as magnitude of the chirality-induced contributions to the anomalous and spin Hall conductivities has been demonstrated. Similar calculations of the spin-orbit torque and the Edelstein polarization reveal sizable topological contributions also here, that can, depending on which quantity and which tensor element is considered as well as on the polar angle, enhance or suppress the spin-orbit-induced effects and be either dominating or vanishing.

Future studies on realistic non-collinear antiferromagnets of the hexagonal Mn_3X type with $\text{X} = \text{Ga}, \text{Ge},$ or Sn based on the experimentally assumed or theoretically proposed spin structures could help determining the actual configuration and the relevance of chirality-induced contributions in measured response properties. A proposed extension of the XMCD sum rules to non-collinear magnetic order and the absence of spin-orbit coupling should be able to support experimental efforts on the quantification of topological orbital moments.

ACKNOWLEDGMENTS

Financial support by the DFG via SFB 1277 (*Emergente relativistische Effekte in der Kondensierten Materie*) is gratefully acknowledged.

Appendix A: Manipulating the spin-orbit coupling

The topological contributions to the various response quantities discussed were determined by either setting the spin-orbit coupling explicitly to zero in the self-consistent calculations (when dealing with the orbital magnetic moment) or by scaling the speed of light c in the X-ray absorption and Kubo linear response calculations. The limit $c_0/c \rightarrow 0$ with the speed of light in vacuum c_0 , or equivalently $c/c_0 \rightarrow \infty$, corresponds to the non-relativistic case. Obviously not only the spin-orbit coupling is affected this way, but also the so-called scalar-relativistic effects. However, for the properties relevant to this work the spin-orbit coupling is the relevant relativistic correction.

Figure 18 shows the anomalous (black symbols) and spin Hall (red symbols) conductivities as a function of the scaled speed of light c_0/c for the ferromagnetic state (top), the non-coplanar magnetic state ncpM0 depicted in the top panel of Fig. 4 (middle), and the coplanar non-collinear antiferromagnetic state ncAFM0 (bottom). Going from the relativistic limit on the right side to the non-relativistic on the left, both σ_{xy} and σ_{xy}^z vanish for the ferromagnet, revealing their purely SOC-driven nature. In the non-coplanar magnetic state ($\theta = 45^\circ$) in the middle panel both are finite for $c_0/c \rightarrow 0$, i.e., they exhibit a chirality-induced or topological contribution arising from

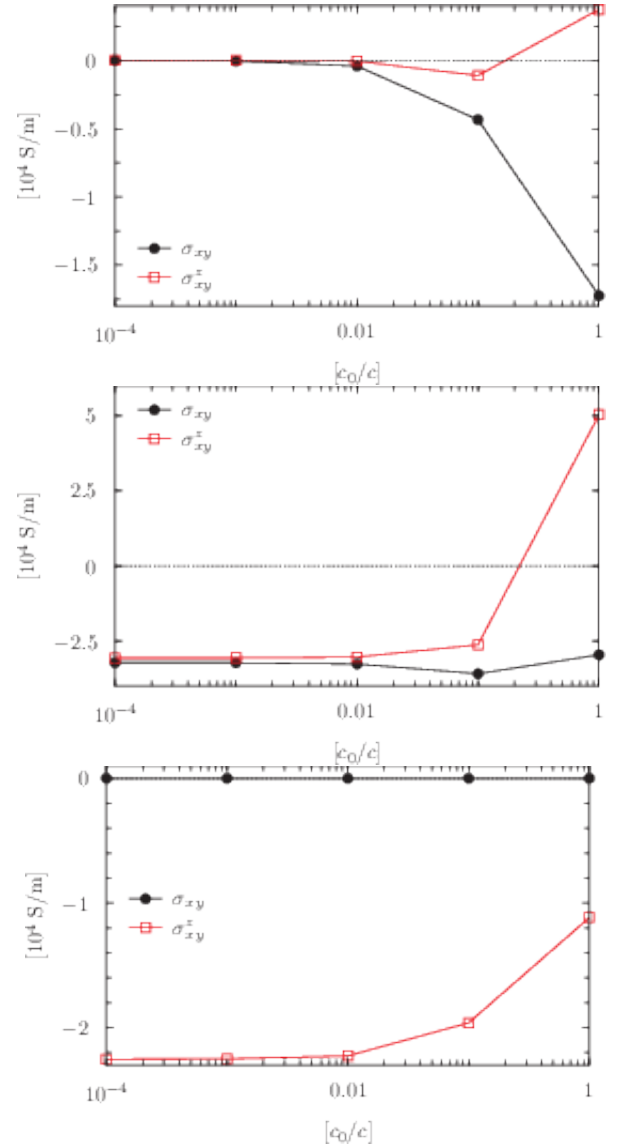


FIG. 18. Anomalous and spin Hall conductivity as a function of c_0/c in the ferromagnetic state (top), the non-coplanar chiral magnetic state ncpM0 (middle) for $\theta = 45^\circ$, and the coplanar non-collinear chiral state ncAFM0 (bottom). The relativistic limit is on the right ($c_0/c = 1$), the non-relativistic one on the left ($c_0/c \rightarrow 0$).

the spin texture. For both quantities this is sizable, the so-called topological Hall effect (THE) is even dominating in the relativistic limit, while the topological spin Hall effect (TSHE) is of opposite sign when compared to the SOC-induced contribution and about half as large. For the non-collinear antiferromagnetic structure ncAFM0 in the bottom panel the anomalous Hall effect vanishes due to symmetry (see Table I and Eq. 1), while the TSHE is even larger than the total SHE. This means that here the contribution due to spin-orbit coupling is again of opposite sign and but now the chirality-induced part is about

twice as large.

Corresponding results for the structures ncpM9 (again for $\theta = 45^\circ$) and ncAFM9 are presented in Fig. 19. Here the relation of chirality- and SOC-induced contributions is somewhat different. The former is smaller and of opposite sign for the AHE, while of the same sign for the SHE in the non-coplanar magnetic structure (top). In the coplanar antiferromagnetic state (bottom) the AHE is again vanishing, whereas the SHE is predominantly chirality-induced.

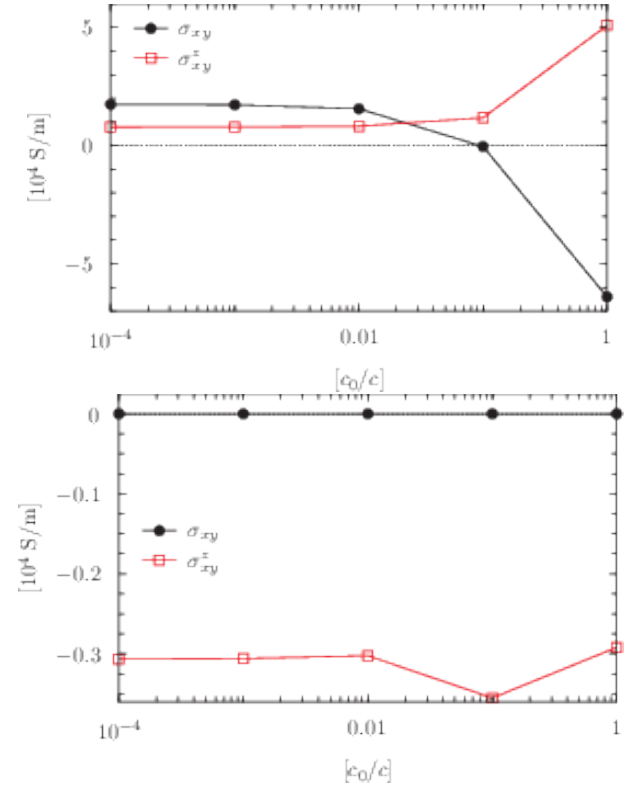


FIG. 19. Anomalous and spin Hall conductivity as a function of c_0/c in the non-coplanar achiral magnetic state ncpM9 (top) for $\theta = 45^\circ$, and the co-planar non-collinear achiral state ncAFM9 (bottom). The relativistic limit is on the right ($c_0/c = 1$), the non-relativistic one on the left ($c_0/c \rightarrow 0$).

- ¹ M. Bode, M. Heide, K. von Bergmann, P. Ferriani, S. Heinze, G. Bihlmayer, A. Kubetzka, O. Pietzsch, S. Blügel, and R. Wiesendanger, *Nature* **447**, 190 (2007).
- ² C. Train, R. Gheorghe, V. Krstic, L.-M. Chamoreau, N. S. Ovanesyan, G. L. J. A. Rikken, M. Gruselle, and M. Verdaguer, *Nature Materials* **7**, 729 (2008).
- ³ H.-B. Braun, *Advances in Physics* **61**, 1 (2012).
- ⁴ J. Stein, M. Baum, S. Holbein, T. Finger, T. Cronert, C. Tölzer, T. Fröhlich, S. Biesenka, K. Schmalzl, P. Steffens, C. H. Lee, and M. Braden, *Phys. Rev. Lett.* **119**, 177201 (2017).
- ⁵ C. S. Spencer, J. Gayles, N. A. Porter, S. Sugimoto, Z. Aslam, C. J. Kinane, T. R. Charlton, F. Freimuth, S. Chadov, S. Langridge, J. Sinova, C. Felser, S. Blügel, Y. Mokrousov, and C. H. Marrows, *Phys. Rev. B* **97**, 214406 (2018).
- ⁶ T. Skyrme, *Nuclear Physics* **31**, 556 (1962).
- ⁷ S. Mühlbauer, B. Binz, F. Jonietz, C. Pfleiderer, A. Rosch, A. Neubauer, R. Georgii, and P. Böni, *Science* **323**, 915 (2009).
- ⁸ A. Neubauer, C. Pfleiderer, B. Binz, A. Rosch, R. Ritz, P. G. Niklowitz, and P. Böni, *Phys. Rev. Lett.* **102**, 186602 (2009), erratum: *Phys. Rev. Lett.* **110**, 209902 (2013).
- ⁹ S. Heinze, K. von Bergmann, M. Menzel, J. Brede, A. Kubetzka, R. Wiesendanger, G. Bihlmayer, and S. Blügel, *Nat. Phys.* **7**, 713 (2011).
- ¹⁰ B. Dupe, M. Hoffmann, C. Paillard, and S. Heinze, *Nature Communications* **5**, 4030 (2014).
- ¹¹ H. Reichlová, D. Kriegner, V. Holý, K. Olejník, V. Novák, M. Yamada, K. Miura, S. Ogawa, H. Takahashi, T. Jungwirth, and J. Wunderlich, *Phys. Rev. B* **92**, 165424 (2015).
- ¹² C. Moreau-Luchaire, C. Moutas, N. Reyren, J. Sampaio, C. A. F. Vaz, N. Van Horne, K. Bouzehouane, K. Garcia, C. Deranlot, P. Warnicke, P. Wohlhüter, J.-M. George, M. Weigand, J. Raabe, V. Cros, and A. Fert, *Nature Nanotechnology* **11**, 444 (2016).
- ¹³ S. Woo, K. Litzius, B. Krüger, M.-Y. Im, L. Caretta, K. Richter, M. Mann, A. Krone, R. M. Reeve, M. Weigand, P. Agrawal, I. Lemes, M.-A. Mawass, P. Fischer, M. Kläui, and G. S. D. Beach, *Nature Materials* **15**, 501 (2016).
- ¹⁴ A. K. Nayak, V. Kumar, T. Ma, P. Werner, E. Pippel, R. Sahoo, F. Damay, U. K. Rößler, C. Felser, and S. S. P. Parkin, *Nature* **548**, 561 (2017).
- ¹⁵ X. Z. Yu, N. Kanazawa, W. Z. Zhang, T. Nagai, T. Hara, K. Kimoto, Y. Matsui, Y. Onose, and Y. Tokura, *Nature*

- Communications **3**, 988 (2012).
- ¹⁶ J. Sampaio, V. Cros, S. Rohart, A. Thiaville, and A. Fert, *Nature Nanotechnology* **8**, 839 (2013).
 - ¹⁷ A. Fert, V. Cros, and J. Sampaio, *Nature Nanotechnology* **8**, 152 (2013).
 - ¹⁸ R. Tomasello, E. Martinez, R. Zivieri, L. Torres, M. Carpentieri, and G. Finocchio, *Scientific Reports* **4**, 6784 (2014).
 - ¹⁹ A. Fert, N. Reyren, and V. Cros, *Nature Reviews Materials* **2**, 17031 (2017).
 - ²⁰ W. Koshibae and N. Nagaosa, *Nature Communications* **7**, 10542 (2016).
 - ²¹ R. Shindou and N. Nagaosa, *Phys. Rev. Lett.* **87**, 116801 (2001).
 - ²² K. Nakamura, T. Ito, and A. J. Freeman, *Phys. Rev. B* **68**, 180404 (2003).
 - ²³ M. Hoffmann, J. Weischenberg, B. Dupé, F. Freimuth, P. Ferriani, Y. Mokrousov, and S. Heinze, *Phys. Rev. B* **92**, 020401 (2015).
 - ²⁴ J.-P. Hanke, F. Freimuth, A. K. Nandy, H. Zhang, S. Blügel, and Y. Mokrousov, *Phys. Rev. B* **94**, 121114 (2016).
 - ²⁵ M. dos Santos Dias, J. Bouaziz, M. Bouhassoune, S. Blügel, and S. Lounis, *Nature Communications* **7**, 13613 (2016).
 - ²⁶ J.-P. Hanke, F. Freimuth, S. Blügel, and Y. Mokrousov, *Scientific Reports* **7**, 41078 (2017).
 - ²⁷ Y. Taguchi, Y. Oohara, H. Yoshizawa, N. Nagaosa, and Y. Tokura, *Science* **291**, 2573 (2001).
 - ²⁸ G. Tatara and H. Kawamura, *J. Phys. Soc. Japan* **71**, 2613 (2002).
 - ²⁹ M. Onoda and N. Nagaosa, *Journal of the Physical Society of Japan* **71**, 19 (2002).
 - ³⁰ P. Bruno, V. K. Dugaev, and M. Taillefumier, *Phys. Rev. Lett.* **93**, 096806 (2004).
 - ³¹ T. Tomizawa and H. Kontani, *Phys. Rev. B* **82**, 104412 (2010).
 - ³² T. Schulz, R. Ritz, A. Bauer, M. Halder, M. Wagner, C. Franz, C. Pfleiderer, K. Everschor, M. Garst, and A. Rosch, *Nature Physics* **8**, 301 (2012).
 - ³³ N. Nagaosa and Y. Tokura, *Nature Nanotechnology* **8**, 899 (2013).
 - ³⁴ C. Franz, F. Freimuth, A. Bauer, R. Ritz, C. Schnarr, C. Duvinage, T. Adams, S. Blügel, A. Rosch, Y. Mokrousov, and C. Pfleiderer, *Phys. Rev. Lett.* **112**, 186601 (2014).
 - ³⁵ G. Yin, Y. Liu, Y. Barlas, J. Zang, and R. K. Lake, *Phys. Rev. B* **92**, 024411 (2015).
 - ³⁶ P. M. Buhl, F. Freimuth, S. Blügel, and Y. Mokrousov, *physica status solidi (RRL) Rapid Research Letters* **11**, 1700007 (2017), 1700007.
 - ³⁷ H. Chen, Q. Niu, and A. H. MacDonald, *Phys. Rev. Lett.* **112**, 017205 (2014).
 - ³⁸ J. Kübler and C. Felser, *EPL (Europhysics Letters)* **108**, 67001 (2014).
 - ³⁹ Y. Zhang, Y. Sun, H. Yang, J. Železný, S. P. P. Parkin, C. Felser, and B. Yan, *Phys. Rev. B* **95**, 075128 (2017).
 - ⁴⁰ D. Boldrin and A. S. Wills, *Advances in Condensed Matter Physics* **2012**, 615295 (2012).
 - ⁴¹ C. Sürgers, G. Fischer, P. Winkel, and H. v. Löhneysen, *Nature Communications* **5**, 3400 (2014).
 - ⁴² S. Nakatsuji, N. Kiyohara, and T. Higo, *Nature* **527**, 212 (2015).
 - ⁴³ N. Kiyohara, T. Tomita, and S. Nakatsuji, *Phys. Rev. Applied* **5**, 064009 (2016).
 - ⁴⁴ A. K. Nayak, J. E. Fischer, Y. Sun, B. Yan, J. Karel, A. C. Komarek, C. Shekhar, N. Kumar, W. Schnelle, J. Kübler, C. Felser, and S. S. P. Parkin, *Sci. Adv.* **2**, e1501870 (2016).
 - ⁴⁵ C. Sürgers, T. Wolf, P. Adelman, W. Kittler, G. Fischer, and H. v. Löhneysen, *Scientific Reports* **7**, 42982 (2017).
 - ⁴⁶ Z. H. Liu, Y. J. Zhang, G. D. Liu, B. Ding, E. K. Liu, H. M. Jafri, Z. P. Hou, W. H. Wang, X. Q. Ma, and G. H. Wu, *Scientific Reports* **7**, 515 (2017).
 - ⁴⁷ J. Orenstein and J. E. Moore, *Phys. Rev. B* **87**, 165110 (2013).
 - ⁴⁸ W. Feng, G.-Y. Guo, J. Zhou, Y. Yao, and Q. Niu, *ArXiv e-prints* (2015), arXiv:1509.02865 [cond-mat.mtrl-sci], arXiv:1509.02865 [cond-mat.mtrl-sci].
 - ⁴⁹ S. Wimmer, J. Minár, S. Mankovsky, A. N. Yaresko, and H. Ebert, “Magneto-optic and transverse transport properties of noncollinear antiferromagnets,” unpublished (2018).
 - ⁵⁰ O. Gomonay, *Phys. Rev. B* **91**, 144421 (2015).
 - ⁵¹ J. Železný, Y. Zhang, C. Felser, and B. Yan, *Phys. Rev. Lett.* **119**, 187204 (2017).
 - ⁵² Y. Zhang, J. Zelezny, Y. Sun, J. van den Brink, and B. Yan, *ArXiv e-prints* (2017), arXiv:1704.03917 [cond-mat.mtrl-sci].
 - ⁵³ J. B. S. Mendes, R. O. Cunha, O. Alves Santos, P. R. T. Ribeiro, F. L. A. Machado, R. L. Rodríguez-Suárez, A. Azevedo, and S. M. Rezende, *Phys. Rev. B* **89**, 140406 (2014).
 - ⁵⁴ W. Zhang, W. Han, S.-H. Yang, Y. Sun, Y. Zhang, B. Yan, and S. S. P. Parkin, *Sci. Adv.* **2**, e1600759 (2016).
 - ⁵⁵ G.-Y. Guo and T.-C. Wang, *Phys. Rev. B* **96**, 224415 (2017).
 - ⁵⁶ M. Ikhlas, T. Tomita, T. Koretsune, M.-T. Suzuki, D. Nishio-Hamane, R. Arita, Y. Otani, and S. Nakatsuji, *Nat. Phys.* **13**, 1085 (2017).
 - ⁵⁷ L. Šmejkal, Y. Mokrousov, B. Yan, and A. H. MacDonald, *Nature Physics* **14**, 242 (2018).
 - ⁵⁸ W. H. Kleiner, *Phys. Rev.* **142**, 318 (1966).
 - ⁵⁹ M. Seemann, D. Ködderitzsch, S. Wimmer, and H. Ebert, *Phys. Rev. B* **92**, 155138 (2015).
 - ⁶⁰ S. Wimmer, K. Chadova, M. Seemann, D. Ködderitzsch, and H. Ebert, *Phys. Rev. B* **94**, 054415 (2016).
 - ⁶¹ S. Wimmer, K. Chadova, and H. Ebert, “Symmetry and magnitude of the direct and inverse Edelstein effect: A KKR-CPA-Kubo approach,” unpublished (2018).
 - ⁶² H. T. Stokes, D. M. Hatch, and B. J. Campbell, *ISOTROPY Software Suite*, iso.byu.edu.
 - ⁶³ H. T. Stokes and D. M. Hatch, *J. Appl. Crystallogr.* **38**, 237 (2005).
 - ⁶⁴ R. Kubo, *Can. J. Phys.* **34**, 1274 (1956).
 - ⁶⁵ R. Kubo, *J. Phys. Soc. Japan* **12**, 570 (1957).
 - ⁶⁶ W. H. Butler, *Phys. Rev. B* **31**, 3260 (1985).
 - ⁶⁷ A. Crépieux and P. Bruno, *Phys. Rev. B* **64**, 014416 (2001).
 - ⁶⁸ D. Ködderitzsch, K. Chadova, and H. Ebert, *Phys. Rev. B* **92**, 184415 (2015).
 - ⁶⁹ *The Munich SPR-KKR package*, H. Ebert *et al.*
<http://olymp.cup.uni-muenchen.de/ak/eibert/SPRKKR>.
 - ⁷⁰ H. Ebert, *Rep. Prog. Phys.* **59**, 1665 (1996).
 - ⁷¹ P. Středa, *J. Phys. C: Solid State Phys.* **15**, L717 (1982).
 - ⁷² This figure has been created using the software VESTA⁸⁴.
 - ⁷³ D. Zhang, B. Yan, S.-C. Wu, J. Kübler, G. Kreiner, S. S. P. Parkin, and C. Felser, *J. Phys.: Cond. Mat.* **25**, 206006 (2013).
 - ⁷⁴ *International Tables for Crystallography, Volume A: Space*

- Group Symmetry* (Springer, 2002).
- ⁷⁵ The sum over all sites is shown, which leaves only the z-component non-zero.
 - ⁷⁶ J. L. Erskine and E. A. Stern, Phys. Rev. B **12**, 5016 (1975).
 - ⁷⁷ B. T. Thole, P. Carra, F. Sette, and G. van der Laan, Phys. Rev. Lett. **68**, 1943 (1992).
 - ⁷⁸ P. Carra, B. T. Thole, M. Altarelli, and X. Wang, Phys. Rev. Lett. **70**, 694 (1993).
 - ⁷⁹ H. Ebert, S. Mankovsky, K. Chadova, S. Polesya, J. Minár, and D. Ködderitzsch, Phys. Rev. B **91**, 165132 (2015).
 - ⁸⁰ M. V. Berry, Proceedings of the Royal Society of London A: Mathematical, Physical and Engineering Sciences **392**, 45 (1984).
 - ⁸¹ D. Xiao, M.-C. Chang, and Q. Niu, Rev. Mod. Phys. **82**, 1959 (2010).
 - ⁸² K. Nakazawa and H. Kohno, Journal of the Physical Society of Japan **83**, 073707 (2014).
 - ⁸³ H. Ishizuka and N. Nagaosa, Sci. Adv. **4**, aap9962 (2018).
 - ⁸⁴ K. Momma and F. Izumi, J. Appl. Crystallogr. **44**, 1272 (2011).